Title

Suppressing the Dark Current in Quantum Dot Infrared Photodetectors by Controlling Carrier Statistics

Journal

Advanced Optical Materials, 10(2)

ISSN

2195-1071

Authors

Jung, Byung Ku
Woo, Ho Kun
Shin, Chanho
et al.

Publication Date

2022

DOI

10.1002/adom.202101611

Peer reviewed

ADVANCED OPTICAL MATERIALS
www.advopticalmat.de

Suppressing the Dark Current in Quantum Dot Infrared Photodetectors by Controlling Carrier Statistics

Byung Ku Jung, Ho Kun Woo, Chanho Shin, Taesung Park, Ning Li, Kyu Joon Lee, Woosik Kim, Jung Ho Bae, Jae-Pyoung Ahn, Tse Nga Ng, and Soong Ju Oh**

Lead sulfide colloidal quantum dot photodiodes (PbS QDPDs) exhibit a high energy conversion efficiency for infrared detection. Despite the high photoinduced current, the performance of PbS QDPDs is limited by the high dark current which is rarely investigated. Understanding the dark current in PbS QDPDs is critical to improving the detectivity of PbS QDPDs. Herein, it is demonstrated that minority carriers of I-passivated PbS films and trap sites of EDT-passivated PbS films are related to the dark current of PbS QDPD. Utilizing annealing and low-temperature ligand exchange processes, the dark current density can be decreased almost tenfold by suppressing the minority carrier diffusion in the PN junction and trap-assisted charge injection from the electrode. PN junction simulation, space charge limited current measurements, as well as structural, optical, and chemical characterizations are conducted to elucidate the origins of the dark current suppression. The authors achieve the lowest dark current density of 2.9×10^{-5} mA cm^{-2} at –1 V among PbS-based QDPDs and a high detectivity of 6.7×10^{12} Jones at 980 nm. It is believed that this work provides fundamental understanding of carrier statistics in nanomaterials and device performance as well as a technological basis for realizing low-cost high-performance optoelectronic devices.

1. Introduction

Infrared (IR) photodetectors have attracted significant attention owing to their potential applications in lidar sensors in driverless vehicles, optical communications, security systems, and biological sensing. Lead sulfide quantum dots (PbS QDs) are promising materials for infrared photodetectors because of their size-tunable band gap in the near-to-mid infrared region, low exciton binding energy, high hole and electron mobilities, and low-temperature solution-based processability.[1–3] To date, PbS QD infrared photodetectors have been developed with various devices such as phototransistors,[4–6] photoconductors,[7–10] and photodiodes (PDs).[3,11–18] In particular, recent studies have focused on PbS quantum dot photodiode (QDPD) structures because of their high energy conversion efficiency[18–20] and high response speed.[11,21,22] To achieve high-performance PbS QDPDs, many studies have been conducted to improve the photon–electron conversion efficiency in the devices based on n$^+$-n–p architecture— for example, with ZnO thin films serving as the electron transport layer (ETL), halide-passivated PbS CQD (PbS-halide) thin films as the active layer, and ethanedithiol (EDT)-passivated PbS (PbS-EDT) CQD thin films as the hole transport layer (HTL). Extensive studies have been conducted to improve light absorbance by utilizing the microcavity effect of oxide/metal/oxide multilayers,[23] plasmonic effect of metal nanostructures,[24,25] and blade coating which increases the active layer thickness.[26,27] Energy band engineering and doping strategies have also been developed between the n$^+$-n and the n–p junction to effectively dissociate the generated exciton by doping ZnO with K or Cs[28,29] and PbS with halide.[30] Post-chemical treatment,[15,31] or surface passivation methods,[13,18] have been investigated to improve the carrier mobility and lifetime for efficient charge transport. To achieve efficient charge collection and improve the sensitivity, a buffer layer or interfacial layer between the electrode and charge transport layer has been examined.[32,33]

While extensive research has been conducted to improve photoinduced current and responsivity, relatively few studies investigated the dark current. The performance of a photodiode is commonly characterized by its specific detectivity, defined as $D^* = \frac{R\sqrt{A\Delta f}}{i_{noise}}$, where R is the spectral responsivity, A is the photosensitive device area, Δf is the detection bandwidth, and i_{noise} is the noise current in the device area.[11,34] Because the noise current is mostly governed by the dark current under an applied bias, it is important to suppress the dark current.

B. K. Jung, H. K. Woo, T. Park, W. Kim, J. H. Bae, S. J. Oh
Department of Materials Science and Engineering
Korea University
145, Anam-ro, Seongbuk-gu, Seoul 02841, Republic of Korea
E-mail: sjoh1982@korea.ac.kr
C. Shin, N. Li, T. N. Ng
Materials Science Engineering Program and Department of Electrical and Computer Engineering
University of California San Diego
La Jolla, CA 92093, USA
E-mail: tnn046@eng.ucsd.edu
K. J. Lee, J.-P. Ahn
Advanced Analysis Center
Korea Institute of Science and Technology
5 Hwarang-ro 14-gil, Seongbuk-gu, Seoul 02792, Republic of Korea
The ORCID identification number(s) for the author(s) of this article can be found under https://doi.org/10.1002/adom.202101611.

DOI: 10.1002/adom.202101611

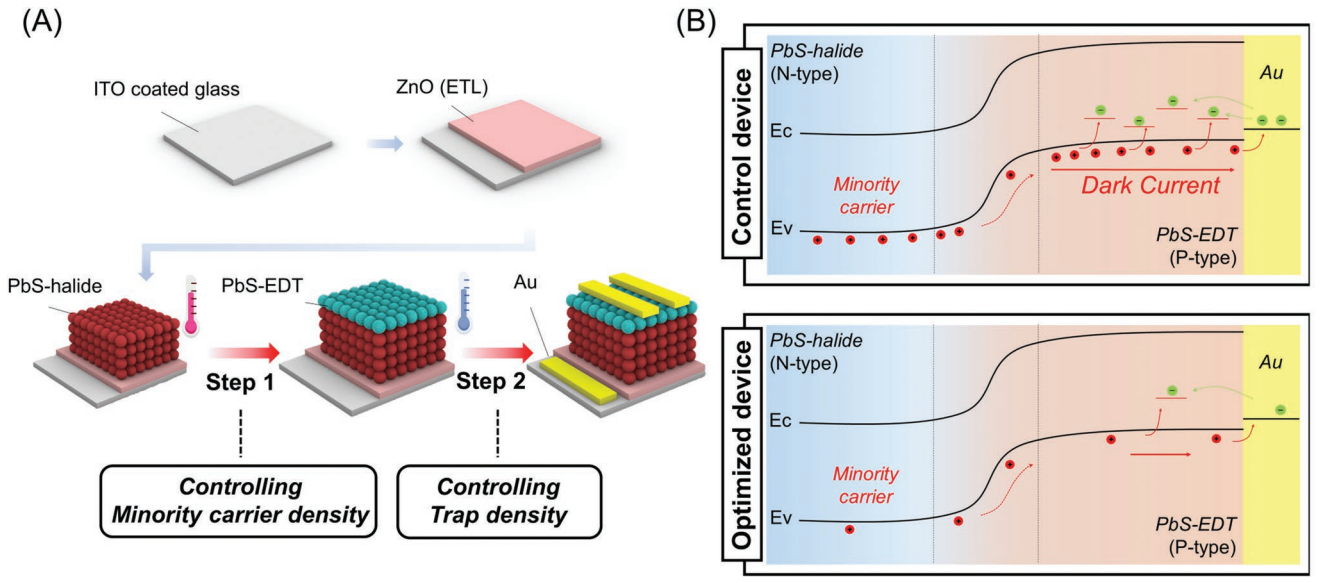

Figure 1. A) Schematic for controlling the minority carrier and trap site density in the PbS QDPD fabrication process. B) The charge transport mechanism of dark current in control device and optimized device.

According to previous studies, there are two main contributions to high dark current. One of the common origins of dark currents is the diffusion of minority carriers. When a reverse bias is applied, unlike a majority carrier, minority carriers easily diffuse across the built-in potential, contributing to the leakage current.[35–38] On the other hand, the dark current can also be generated through trap-assisted charge injection from the electrode to the charge transport layer.[34,39–41] When the trap sites of the charge transport layer are at a deep trap energy level, more charges are injected from the electrode into the PbS layer. In this respect, in the optimal PbS QDPD, dark current can be generated by the minority carriers of the PbS-halide film and trap sites of the PbS–EDT film. The n-type characteristics of PbS halide films are often suppressed by surface oxidation, creating many minority carriers. Under reverse bias, they readily diffuse to the PbS–EDT layer and Au electrode, increasing the leakage current. Poorly passivated PbS–EDT thin films also create many deep trap states in the forbidden band, which increase the leakage current due to undesirable injection from Au electrodes.

In this work, we investigated the origins of dark current in PbS QDPD as a function of minority carrier density in PbS–halide thin films and trap site density in PbS–EDT films. We adopted a post-deposition annealing process to control the electronic properties and carrier statistics of the films (**Figure 1**A). Combinational studies of chemical, optical, and structural analyses, as well as p–n junction stimulation and space charge limited current (SCLC) analysis were conducted to determine the correlation between the surface states of PbS, minority carriers, trap density, and dark current. The results show that the dark current can be suppressed by minimizing the minority carrier and trap site densities. Optimization of the fabrication processes using a newly developed low-temperature ligand exchange (LTLE) process was shown to minimize the dark current of PbS QDPD through treatments by suppressing the minority carrier (SMC) and suppressing trap density (STD) (Figure 1B). Optimized PbS QDPDs showed a dark current density of 2.9×10^{-5} mA cm^{-2} at −1 V, which is the lowest dark current measured among PbS QDPDs to the best of the author's knowledge. The device exhibited a low noise current (2×10^{-12} A Hz$^{-0.5}$) and high detectivity (6.7×10^{12} Jones) at 300 Hz at −3 V bias. Finally, we fabricated 4 × 4 photodiode arrays to demonstrate the improvement in the performance and potential applications in IR image sensor systems.

2. Results and Discussion

Figure 1A shows the overall fabrication process of the PbS QDPD with an ITO/ZnO(ETL)/PbS–halide/PbS-EDT(HTL)/Au structure. A 4 nm PbS quantum dot with the 1st exciton peak at 980 nm was used for the PbS–halide and PbS–EDT layers. (Figure S1, Supporting Information). First, ZnO nanoparticle thin films were deposited onto an ITO-coated glass substrate. As seen in the Experimental Section, the PbS–halide layer and PbS–EDT layer were prepared using the solution ligand exchange and solid ligand exchange methods, respectively, and subsequently spin-coated onto the ZnO layer. Finally, the Au electrode was deposited using thermal evaporation. During the fabrication process, we inserted two steps to control the minority carrier density of the PbS–halide layer and the trap density of PbS–EDT through sequential annealing indicated by the red arrows in Figure 1A. All annealing processes were conducted in air for 30 min.

To examine the effect of the annealing process on each layer, eight samples were prepared: PbS–halide film without annealing and with annealing at 80 °C, 120 °C, and 160 °C and PbS–EDT film without annealing and with annealing at 80 °C, 120 °C, and 160 °C. These layers are denoted as halide-w/o, halide-80 °C, halide-120 °C, halide-160 °C, EDT-w/o, EDT-80 °C, EDT-120 °C, and EDT-160 °C. Furthermore, we conducted LTLE process on PbS–EDT, denoted as EDT-0 °C.

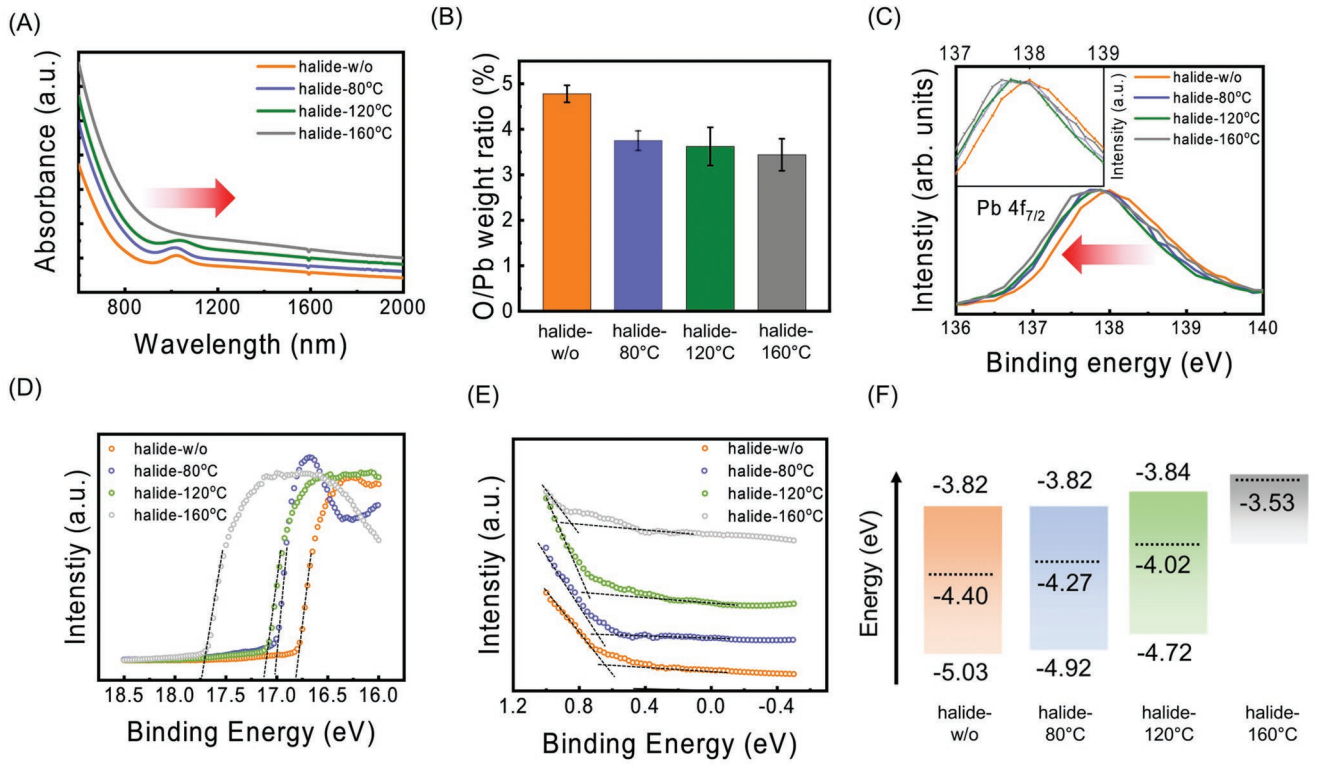

Figure 2. A) UV–vis spectrum of the prepared PbS–halide thin films: (orange) halide-w/o, (blue) halide-80 °C, (olive) halide-120 °C, (gray) halide-160 °C. B) O/Pb weight ratio of films obtained using SEM-EDS measurement. C) XPS spectra, and UPS spectra of the D) cut-off and E) onset region for each PbS–halide film. F) The total band diagram transition of PbS–halide thin films subjected to different post-deposition annealing treatments.

The effect of the annealing temperature on the optical properties of the PbS–halide layers was investigated via UV–vis spectra, as shown in **Figure 2**A. The halide-w/o film exhibited a 1st exciton peak at 1020 nm, which is red shifted from the peak of the PbS QDs (980 nm). This is attributed to the increased coupling effect as the ligand exchange process decreases the distance between the QDs. The 1st excitonic peak remained at an almost similar position, 1020 nm, upon annealing at 80 °C and red shifted to 1045 nm at 120 °C. The peak broadens as the temperature increases, and finally, at 160 °C, the peak disappears. The red shift and broadening are attributed to the sintering effect upon annealing. The loss of 1st excitonic peak at 160 °C indicates that the QDs were completely sintered into large particles, in which the quantum confinement effect disappeared. Similar trends were observed in the TEM analysis and XRD analysis, where annealing at high temperature resulted in the sintering of PbS QDs (Figure S2, Supporting Information). Figure S3, Supporting Information, shows the FTIR spectra of the PbS halide films. The C—H stretching peak of oleic acid (OA) at ≈2900 cm^{-1} disappeared after ligand exchange, and there were no meaningful changes with the annealing treatment.

To investigate the surface state and compositional change of QDs, energy dispersive X-ray spectroscopy (EDS) and X-ray photoelectron spectroscopy (XPS) were conducted. Figure 2B shows the weight ratio of oxygen to lead in the PbS–halide films measured using EDS. As the annealing temperature increased, the O/Pb weight ratio decreased in the following order: halide-w/o (4.78%) > halide-80 °C (3.74%) > halide-120 °C (3.62%) > halide-160 °C (3.44%). This implies that annealing at high temperatures decreases the oxygen component in the PbS–halide QD layers. The PbS $4f_{7/2}$ peak was analyzed from the XPS measurements. As the annealing temperature increased, the peak shifted from 138 to 137.75 eV, 137.75 eV, and 137.63 eV upon annealing at 80 °C, 120 °C, and 160 °C, respectively. The PbS $4f_{7/2}$ peak can be split into two components at 137.5 and 139 eV, corresponding to the binding force of Pb—O and Pb—S.[42] The peak shift to a lower energy indicates an increase in Pb—S binding and a decrease in Pb—O binding on the QD surface (Figure S4, Supporting Information), which agrees well with the EDS measurement. We suppose that the decrease in the oxygen-to-lead ratio results from a mild sintering effect between the PbS QDs. It has been reported that PbS quantum dots (≈4 nm in size) have dominant cation-rich (111) surfaces and a few electrically neutral (100) surfaces.[2,43,44] The (100) surface of PbS QDs is known to be less densely passivated with ligands, allowing this facet to readily oxidize or fuse with other QDs.[45,46] As a result, the mild sintering effect between QDs accelerates fusion between the (100) surfaces, which eliminates the Pb—O binding site on the surface of QDs and increases Pb—S binding between QDs, consistent with the UV–vis spectra in Figure 2A and TEM images (Figure S5, Supporting Information). The halide-to-lead weight ratio of the PbS–halide film, which is mainly related to the (111) facet, does not significantly change with an increase in the annealing temperature (Table S1, Supporting Information).

We conducted ultraviolet photoelectron spectroscopy (UPS) analyses to examine the electronic properties of the PbS–halide films (Figure 2D,E). The positions of the Fermi level and valence band were obtained from the cut-off region and the onset region of the UPS (Figure 2D,E). The Fermi levels of the halide-w/o, halide-80 °C, and halide-120 °C were located at 4.40, 4.27, and 4.02 eV, respectively. The valence band edges of halide-w/o, halide-80 °C, and halide-120 °C were positioned at 3.82, 3.82, and 3.84 eV, respectively. The bandgaps of the PbS–halide upon annealing were obtained from the UV–vis spectra shown in Figure 2A, and the total energy band schemes are depicted in Figure 2F. Notably, PbS–halide-160 °C lost the quantum confinement effect, indicating a significant reduction in the bandgap, which corresponds well with the UV–vis/TEM analysis.

According to the calculated band structure, the Fermi levels moved to the upper levels compared to the valence band maximum as the post-deposition annealing temperature increases (Figure 2E). This clearly shows that annealing at high temperatures enhances n-type doping induced by surface oxidation of PbS QDs. Surface oxygen is known to create acceptor states, contributing to the p-doping effect.[47,48] Thereby, the reduction of surface oxygen, as seen in the EDS and XPS results, can be attributed to the enhancement of n-type doping with hole compensation. In fact, enhancing the n-type characteristic of PbS–halide films results in a relatively reduced minority carrier of the hole carrier density. The hole carrier is inversely proportional to the difference between the Fermi level (E_f) and valance-energy (E_v) levels, according to Equation (1).

$$P_0 = N_v e^{-(E_f - E_v)/kT} \tag{1}$$

where N_v is the effective density of state in valence band, κ is the Boltzmann constant, and T is temperature. The difference between E_f and E_v is 0.63, 0.65, and 0.7 eV in halide-w/o, halide-80 °C, and halide-120 °C, respectively. Therefore, the minority carrier density of the PbS–halide layer decreased as the annealing temperature increased to 120 °C. The effect of the minority carrier density on the dark current is discussed later.

The effect of annealing treatment on the PbS–EDT films was analyzed (Figure 2A–C). PbS–EDT layer annealing was conducted only at 80 °C and 120 °C, as annealing at 160 °C completely sintered the QDs, as in the case with PbS–halide. To measure the change in the optical properties, UV–vis spectra were measured (**Figure 3**A). The EDT-w/o film exhibited a 1st exciton peak at 992 nm, which was red-shifted from the peak of the PbS QDs (980 nm) because of the coupling effect. The 1st exciton peaks of EDT-80 °C and EDT-120 °C were blue-shifted to 965 and 917 nm, respectively. This blue shift phenomenon is typically considered as an enhanced quantum confinement effect associated with a decrease in the size of QDs. To investigate the size change, XRD spectra were analyzed. According to the Scherrer equation, the calculated particle size of EDT-w/o, EDT-80 °C, and EDT-120 °C were 4.43, 4.22, and 3.59 nm,

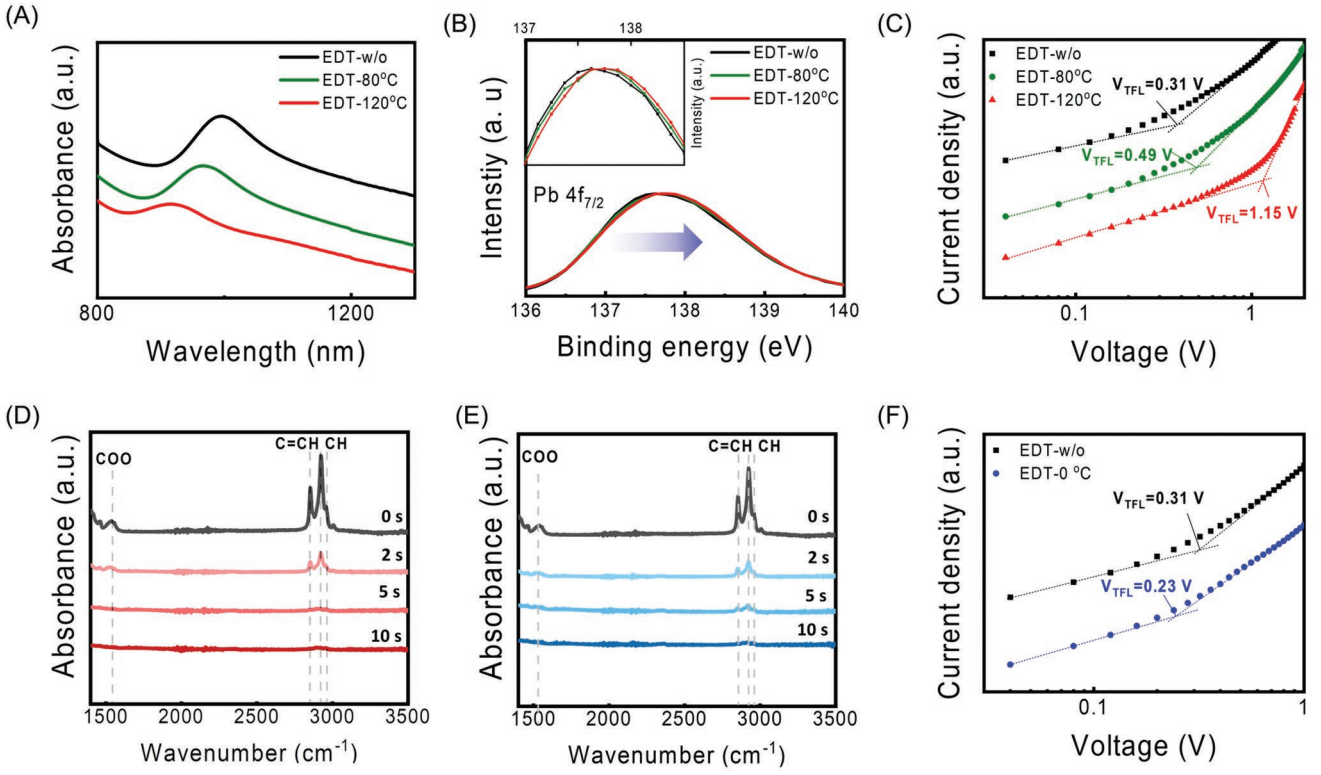

Figure 3. A) UV–vis spectra, B) XPS spectra, and C) SCLC spectra for PbS–EDT thin films (black) without annealing and with (olive) 80 °C and (red) 120 °C annealing. FT-IR spectra for PbS-EDT films before (0 s) and after ligand exchange (2 s, 5 s, 10 s): D) without and E) with LTLE. F) SCLC spectra for PbS–EDT film without (black) and with (blue) LTLE.

respectively, implying that annealing induces the decrease in particle size (Figure S6, Supporting Information).

To investigate the origin of the blue shift of the 1st excitonic peak and the size decrease, EDS and XPS analyses were conducted. EDS analysis showed that as the annealing temperature increased, the O/Pb weight ratio increased in the following order: EDT-w/o (25.55%) > EDT-80 °C (32.59%) > EDT-120 °C (39.22%) (Figure S7, Supporting Information). XPS analysis showed that the XPS peaks of PbS $4f_{7/2}$ showed a blue shift as the annealing temperature increased (Figure 2B). EDT-w/o, EDT-80 °C, and EDT-120 °C exhibited XPS peaks at 137.625, 137.75, and 137.875 eV, respectively. PbS-EDT shows that Pb—O binding increases and Pb—S binding decreases as the annealing temperature increases (Figure S7, Supporting Information). This indicates that the surface of PbS–EDT oxidizes upon annealing, forming a PbO shell. The formation of the PbO shell decreases the core size of PbS, in agreement with the observation of the blue shift of the 1st excitonic peak in the UV–vis measurement. A control experiment under a nitrogen environment was conducted, where the first excitonic peak of PbS–EDT red-shifted upon annealing at 80 °C and 120 °C and disappeared at 160 °C. This confirms that oxygen causes a blue shift in the PbS–EDT film upon annealing (Figure S3, Supporting Information).

Notably, upon annealing, the oxygen component decreased in PbS–halide QDs but increased in PbS–EDT QDs. We attribute this difference to the degree of passivation by inorganic and organic ligands. Indeed, PbS–halide QDs are well passivated with inorganic halide ligands, but PbS–EDT QDs are less densely passivated with organic ligands due to steric hindrance. Inorganic ligands are known to effectively passivate the surface from oxygen, but organic ligands are vulnerable to oxidation. In addition, FTIR measurements showed that upon annealing, the EDT ligand was removed from the QD surface, exposing the non-passivating surface to air and promoting surface oxidation (Figure S8, Supporting Information).

To investigate the trap density of the PbS–EDT films upon annealing, space charge-limited current measurements were conducted (Figure 3C). The hole-only devices (ITO/MoO_3/PbS-EDT/MoO_3/Au) were prepared at different annealing temperatures to quantify the trap site density of the PbS–EDT films. The device shows ohmic contact in the low-voltage region because thermally generated carriers are more dominant than the carriers injected from the electrode. A rapid increase in current injection was observed at a voltage ($>V_{TFL}$), when all the traps in the films are filled. The hole-only devices of EDT-w/o, EDT-80 °C, and EDT-120 °C exhibited V_{TFL} at 0.31, 0.49, and 1.15 V, respectively. The estimated trap density values were 6.16×10^{16} cm^{-3}, 9.749×10^{16} cm^{-3}, and2.29×10^{17} cm^{-3} (details of the calculation are in the Supporting Information). This shows that the trap density of the PbS–EDT film increased during the high-temperature annealing process. The increased trap density in the PbS–EDT film originates from the non-passivating surface states due to the removal of EDT ligands upon annealing.[45]

The electrical characterization revealed that lowering the temperature is important for reducing the trap density in PbS–EDT thin films. Based on this observation, we developed an LTLE process, which involves conducting the ligand exchange process at a low temperature of 0 °C, and applied it to PbS–EDT films, denoted as EDT-0 °C. The effects of LTLE on PbS–EDT films are shown in Figure 3D–F. In Figure 3D,E, FTIR spectra were examined at different exchange times to investigate the ligand exchange speed of EDT-w/o and EDT-0 °C. In the case of EDT-w/o, the intensity of the C—H stretching peaks was reduced by more than 95% after 5 s (Figure 3D). However, in the case of EDT-0 °C, the C—H stretching peaks were maintained after 5 s before finally decreasing by more than 95% after 10 s (Figure 3F). This indicates that the exchange process at lower temperatures was slower. To completely exchange the ligand from oleic acid to EDT, the two films were treated with 30 s of ligand exchange (Figure S9, Supporting Information).

The effects of LTLE on the structural properties of the PbS–EDT layer were analyzed using small-angle X-ray scattering (SAXS) spectra and EDS spectra (Figure S10A, Supporting Information). From SAXS analysis, the interdot spaces of EDT-w/o and EDT-0 °C were calculated to be 4.42 and 4.59 nm, respectively, whereas that of as-synthesis PbS thin film was 5.41 nm. The full width at half maximum (FWHM) of EDT-0 °C was smaller than that of EDT-w/o, indicating the improved order of the film. These results are consistent with the UV–vis spectra (Figure S10B, Supporting Information). The 1st exciton peak of EDT-0 °C was located at a shorter wavelength than that of EDT-w/o, indicating an increased interdot spacing in EDT-0 °C. The peak-to-valley ratio of EDT 0 °C was also higher than that of EDT-w/o, indicating the increased uniformity of optical bandgap of quantum dots. As slow-speed ligand exchange can minimize the surface attachment between QDs that occasionally occurs during the ligand exchange process, a higher order with a larger interdot space was achieved. EDS measurements also supported the suppressed attachment between QDs (Figure S10C, Supporting Information).

Finally, SCLC measurements were conducted to quantify the trap site density of the PbS–EDT films (Figure 3F). EDT-w/o and EDT-0 °C exhibited V_{TFL} at 0.31 and 0.23 eV, respectively. The calculated trap site densities of EDT-w/o and EDT-0 °C were 4.57×10^{16} cm^{-3} and 4.457×10^{16} cm^{-3}, respectively. The decreased trap site density of EDT-0 °C resulted from the improvement of surface passivation, as seen in Figure S10C, Supporting Information.

To investigate the effect of annealing treatment on PbS–halide films in dark current density, we fabricated PbS QDPDs using halide-w/o (control device), halide-80 °C, and halide-120 °C. The three devices commonly use EDT-w/o as the PbS–EDT layer. In the UPS analyses shown in Figure 2D–F, we found that the minority carrier density decreased as the annealing temperature increased to 120 °C. Using this result and the *J–V* curve of the control device, we simulated the dark current density of PbS QDPDs as a function of minority carrier density at different annealing temperatures in PbS–halide layers (see the details in the Supporting Information). The simulation predicted that the dark current density decreased under all voltage conditions when the annealing treatment increased (**Figure 4**A). The experimental (solid line) and simulated (dotted line) *J–V* curves of PD with halide-80 °C and PD with halide-120 °C are shown in Figure 4B. The experimental results show that the dark current decreased in the following order:

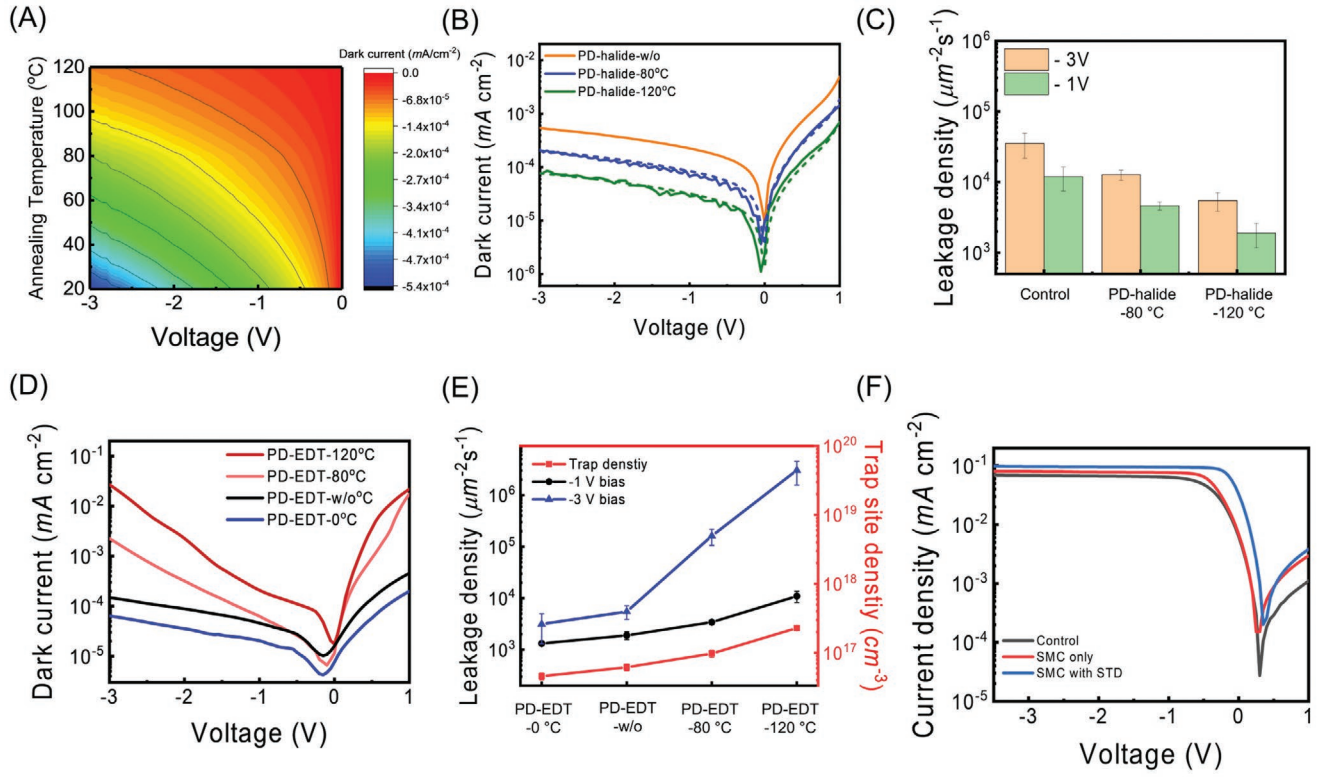

Figure 4. A) Simulation of the dark current density according to annealing temperature and voltage. B) Simulation (dotted lines) and experimental results (solid lines) of the dark current density versus voltage behavior of (orange) PD with halide-w/o (control device), (blue) halide-80 °C, and (olive) halide-120 °C. C) The leakage charge density of the control device, PD with halide-80 °C, and with halide-120 °C were statistically investigated under −3 V and −1 V conditions. D) Experimental results of dark current density of PD with (blue) EDT-0 °C, (black) EDT-w/o, (pink) EDT-80 °C, and (red) EDT-120 °C. E) The relation between leakage charge density under (black) −1 V bias, (blue) −3 V, and (red) trap site density of EDT films. F) The photoinduced current density of the control device, SMC-treated device, and SMC with STD-treated devices at 980 nm with 1.27×10^{-1} mW cm^{-2} intensity.

control device > PD with halide-80 °C > PD with halide-120 °C. In addition, the PbS QDPD fabricated at halide-160 °C exhibited a much higher dark current density than the control device because the halide 160 °C layer experienced complete sintering (Figure S11, Supporting Information). The lowest dark current was achieved under the 120 °C annealing treatment, labeled as the SMC treatment.

To quantitatively measure the dark current density, we evaluated the leakage charge density at −1 V and −3 V, which is the number of charges flowing per unit area and unit time under no illumination. The leakage charge density of the control device, PD with halide-80 °C, and PD with halide-120 °C were statistically calculated from the *J*–*V* curve of 12 different devices for each condition at −3 V and −1 V conditions (Figure 4C; Table S2, Supporting Information). Compared to the control device, the PD with halide-80 °C and PD with halide-120 °C exhibited 2.6 times and 6.35 times lower leakage charge density at −1 V and 2.8 times and 6.49 times lower leakage charge density at −3 V, respectively. In the two-bias condition, the ratio of decreasing dark current density was similar, indicating that the suppressed leakage charge density resulted from the change in the minority carrier density. By annealing PbS–halide, fewer hole carriers are diffused into the depletion layer between PbS–halide and PbS–EDT and collected by the Au electrodes, decreasing the dark current.

To investigate the effect of annealing and LTLE on the PbS–EDT layer on the dark current, a PD with EDT-0 °C, PD with EDT-w/o, PD with EDT-80 °C, and PD with EDT-120 °C were fabricated. Four devices commonly used halide-120 °C as the PbS–halide layer (SMC treatment). In Figure 4D, we measured the *J*–*V* curves of the four devices. Under all voltage conditions, the dark current density increased in the following order: PD with EDT-0 °C < PD with EDT-w/o < PD with EDT-80 °C < PD with EDT-120 °C. The lowest dark current was achieved under the LTLE treatment, which was labeled as STD treatment. In particular, PD with EDT-0 °C exhibited a dark current of 2.9×10^{-5} mA cm^{-2} at −1 V, which is the lowest value for PbS QDPD among those from prior studies, to the best of our knowledge (Table S4, Supporting Information).

The relationship between the leakage current density and trap site density of the four PbS-EDT films is shown in Figure 4D. The leakage current density is shown in Table S3, Supporting Informationand the trap density was obtained from SCLC measurements (Figure 3C,F). We found that the increment ratio of the dark current density was proportionally linear with the change in the trap site density under the −1 V bias condition, resulting from the increasing trap density of the PbS–EDT layer. However, under the −3 V condition, the increment ratio was more rapid than that under −1 V. We attribute this result to the behaviors of trap-assisted charge injection

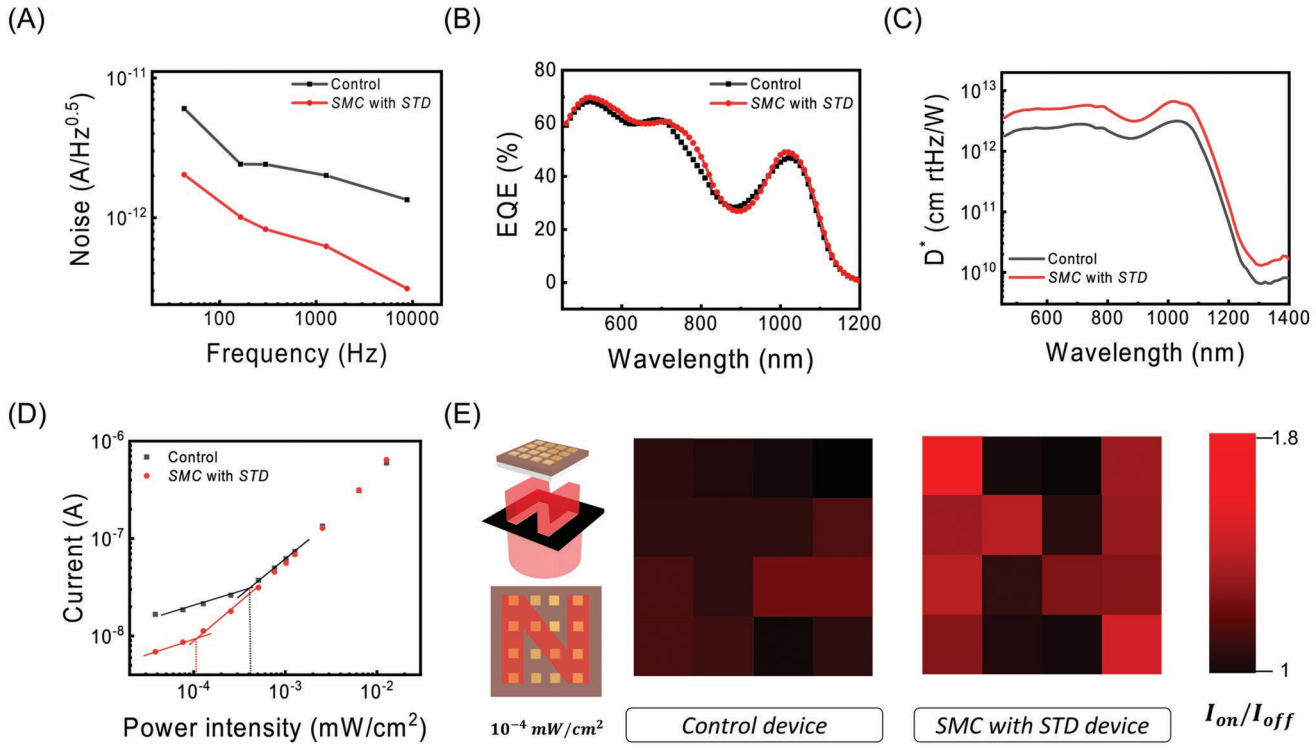

Figure 5. A) Noise frequency spectra, B) EQE spectra, and C) specific detectivity spectrum of the control device (black) and the SMC with STD-treated device (red). D) Input power intensity with 980 nm lasers versus output photocurrent intensity. E) 4 × 4 photodiode array fabricated without any treatment (control device) and SMC with STD-treated device, respectively.

from Au to the PbS-EDT layer (Figure S12, Supporting Information). To inject an electron through the electrical barrier, an electron should overcome the electrical barrier between the trap level of PbS–EDT and the work function of Au, and it would be easier at −3 V than at −1 V because of the reduced electrical barrier (Figure S13, Supporting Information). This phenomenon becomes more prominent if there are more trap states in the PbS–EDT. Indeed, the increase in leakage charge density ratio between −1 and −3 V of PD with EDT-0 °C, EDT-w/o, EDT-80 °C, and EDT-120 °C were calculated to be 2.4, 2.9, 47.4, and 280, respectively. In PD with EDT-80 °C or PD with EDT-120 °C, the leakage current density significantly increased at higher bias as many carriers could be injected because of reduced barriers. However, in LTLE-processed PD with EDT-0 °C, fewer carriers were injected because of the relatively small number of trap sites, even if the barriers were lowered at a high voltage of −3 V bias. This is particularly important because commercial photodiodes have a high operating voltage.

To investigate the effect of SMD and STD treatment on the photoinduced current, we measured the *J*–*V* curve at 980 nm with 1.27×10^{-1}mW cm^{-2} (Figure 4G). The SMC-treated device, which was fabricated with halide-120 °C and EDT-w/o, exhibited a slightly higher photocurrent than the control device. The SMC with the STD-treated device, which was fabricated with halide-120 °C and EDT-0 °C, experienced a significant increase in photocurrent. The improved photocurrent is attributed to the increased mobility and reduced trap density. The average value of responsivity increased in the following order: control (0.53 A W^{-1} at −3 V, 0.50 A W^{-1} at −1 V) < SMC only (0.60 A W^{-1} at −3 V, and 0.56 A W^{-1} at $^{-}$1 V) < SMC with STD (0.65 A W^{-1} at $^{-}$3 V, 0.64 A W^{-1} at $^{-}$1 V) (Figure S14A, Supporting Information). The SMC- and STD-treated devices exhibited the highest I_{on}/I_{off} ratio due to the reduced dark current and increased photocurrent (Figure S14B, Supporting Information). SMC with STD-treated devices showed a 24-fold increment at −3 V and tenfold increment at −1 V compared to control devices. The best device exhibited I_{on}/I_{off} ratios of 3.9×10^3 and 1.34×10^4 at −3 and −1 V, respectively.

To fully characterize the performance of our devices, the noise current, EQE, and specific detectivity *D** were investigated under a −3 V bias at 300 Hz (**Figure 5**A–C). Figure 5A represents measured noise current for both control device and SMC with STD-treated device, which show 2.4×10^{-12} and 8.27×10^{-13} *A* Hz$^{-0.5}$ at 300 Hz, respectively. The EQE of the SMC with the STD-treated device was 50% at 980 nm, which was slightly higher than that of the control device (Figure 5B), consistent with the increased photo-induced current in Figure 4F.

The detectivity can be expressed as

$$D^* = \frac{R\sqrt{A\Delta f}}{i_{noise}} = \frac{e\lambda\sqrt{A\Delta f} * EQE}{hc * i_{noise}} \quad (2)$$

where i_{noise} represents the noise current (Figure 5A), *A* is the active area of the photodiode (≈0.02 cm^2), and Δf is the detection band (313 Hz). The noise current (Figure 5A) and EQE (Figure 5B) were converted into detectivities. The *D** of the control device and SMC with STD treated devices were 6.7×10^{12} Jones and 3.0×10^{12} Jones at 980 nm, respectively. The SMC

with the STD-treated device exhibited a high detectivity of 6.7×10^{12} Jones (Table S4, Supporting Information), which is higher than that of commercial InGaAs photodetectors.

To demonstrate an improvement, we measured the photocurrent in the low-light intensity region and used a 4×4 photodiode array as an image sensor (Figure 5D,E) and optical image of photodiode array is shown in Figure S15, Supporting Information. In Figure 5D, the current was measured as a function of the light intensity at −3 V. The graph of the two devices shows two different regions, with a shallow slope in the first region and a steep slope in the second region. The slope indicates the increment ratio of the photoinduced current (I_{on}) as the light intensity increases, representing the ability to detect light. In the first region, a generated dark current was similar to the photoinduced current, indicating that the PbS QDPD cannot easily measure the photoinduced current. In the second region, photoinduced current was dominant over dark current, indicating that the PbS QDPD can distinguish light intensity. The critical thresholds of the control device and SMC with the STD device were 4.02×10^{-4} and 1.0×10^{-4} mW cm^{-2}, respectively. This means that the SMC and STD-treated devices can detect light intensity values four times lower than those detectable by the control device, owing to the lower dark current density. In Figure 5E, we demonstrate a 4×4 image sensor array, which consists of independent 4×4 PbS QDPDs. Using an "N" patterned mask, we selectively illuminated light with 1.01×10^{-4} mW cm^{-2}. While the control device creates a blurry image, because of the high dark current density, SMC with STD array displayed a clear N pattern.

3. Conclusion

In conclusion, we investigated the effect of the minority carrier of the PbS–halide layer and the trap site of the PbS–EDT layer on the dark current density in PbS QDPD. Through annealing treatment and passivation at low temperature, we precisely controlled the concentration of the minority carrier and trap site density and determined the correlation between the dark current density of PbS QDPD and two factors. By decreasing the minority carrier density in the PbS–halide film and trap site density of the PbS–EDT film, we successfully suppressed the dark current density to 2.9×10^{-5} mA cm^{-2} at −1 V and achieved high detectivity (6.7×10^{12} Jones). This work is a milestone in PbS QDPD studies, provides scientific information on solution-processed photodiodes, and can promote the practical use of PbS QDPDs in various applications, such as lidar, surveillance, and biomedical imaging.

4. Experimental Section

Materials: Lead(II) oxide (PbO) (99.999%) and ammonium acetate (NH_4Ac) were obtained from Alfa Aesar Co. Zinc acetate dihydrate, lead(II) bromide ($PbBr_2$), lead(II) iodide (PbI_2), potassium hydroxide (KOH), oleic acid (OA) (90%), bis(trimethylsilyl)sulfide (TMS_2) (98%), n-octane (99%), 1-octadecene (ODE) (90%), dimethylformamide (DMF), 1,2-ethanedithiol (EDT) (98%), butylamine, and acetonitrile were purchased from Sigma–Aldrich Co. All reagents were used without further purification.

Synthesis of ZnO NPs and PbS QDs: ZnO NPs and PbS QDs were synthesized using the formal Schlenk line technique. ZnO NPs were synthesized using a slightly modified method from a previous study.[49] Zinc acetate dihydrate (2.95 g) was dissolved in methanol (125 mL). The solution was added to a 250 mL three-neck flask and heated to 65 °C. KOH solution (1.48 g in 65 mL methanol) was then slowly added to the flask. The mixture was maintained at 65 °C for 3 h under stirring and then cooled to room temperature via natural cooling. The obtained ZnO NPs were purified three times with methanol using centrifugation at 4500 rpm for 5 min. Purified ZnO NPs were collected in chloroform (50 mg mL^{-1}).

PbS QDs were synthesized using a slightly modified hot injection method from a previous report.[3] A solution of 2.4 g OA, 0.46 g PbO, and 10 mL ODE was degassed in a 100 mL three-neck flask for 30 min under vacuum. Next, the solution was heated for 1 h at 30–120 °C until it became transparent. The solution was then heated to 120 °C under a nitrogen atmosphere. The sulfur precursor (210 µL TMS_2 in 8 mL ODE) in a 5 mL syringe was rapidly injected into the flask. After injection, the solution was cooled to room temperature via natural cooling. The synthesized QDs were washed three times with acetone and ethanol. Finally, the QDs were dispersed in octane (50 mg mL^{-1}).

Ligand Exchange Method: A solution ligand exchange was conducted for PbS–halide layer by a previous reported method with a slight modification.[50] First, lead halides (0.922 g PbI_2 and 0.147 g $PbBr_2$) and 0.0617 g NH_4Ac were dissolved in 20 mL of DMF. Subsequently, 20 mL of the synthesized QDs (10 mg mL^{-1}) was vigorously mixed with the DMF solution. The ligand-exchanged QD solution was washed with octane and centrifuged in toluene. Precipitated QDs were collected using butylamine (200 mg mL^{-1}).

A solid ligand exchange was performed for PbS–EDT layer by a previous reported method.[15] As-synthesized PbS QD (50 mg mL^{-1}) was coated at the speed of 2500 rpm for 30 s and soaked with 0.02 vol% EDT acetonitrile-based solution for 30 s. Then, the films were washed with acetonitrile solution three times to remove residues. These steps were performed three times to deposit the PbS–EDT layers of the optimized thickness.

Fabrication of NIR Photodetector: An indium tin oxide (ITO) glass was cleaned with acetone, isopropanol, and deionized water for 10 min via sonication. The ITO glass was then treated with UV-ozone for 30 min to enhance the adhesion with the ZnO NP layers. ZnO NP layers were spin-coated at 2500 rpm for 30 s. The solution-exchanged PbI2–PbS QDs were then spin-coated onto the ZnO thin films at 2500 rpm for 30 s. Next, the PbS–EDT layer was deposited via the solid exchange method. The as-synthesized OA-capped PbS QDs were coated at a speed of 3000 rpm for 30 s. EDT solution (0.02 vol% in acetonitrile) was applied on the OA-capped PbS QD films for 30 s to exchange the ligand. The films were washed three times with acetonitrile to eliminate residues during the ligand exchange process. The desired thickness of the PbS–EDT layers was achieved by performing these steps twice. An 80 nm-thick Au layer for the anode was deposited on the PbS–EDT layers via thermal evaporation. The area of the device was 4 mm.[2]

Characterization: Current–voltage characteristics were measured using a sourcemeter (Keithley 2400, Tektronix). A UV–vis (Cary5000, Agilent Technologies) spectroscope was used to measure the optical properties of the PbS QD films. Additionally, a field-emission transmission electron microscope (FETEM, G2F30ST, Tecnai, Korea Basic Science Institute) and X-ray diffraction (XRD, D/MAX-2500 V, Rigaku) instrument were used to analyze the structure of the PbS QDs. XPS and UPS (AXIS NOVA, Kratos, Korea Basic Science Institute) instruments were used to analyze the spectra of the PbS QD films coated on the Si substrates and Au deposited on the glass substrates, respectively. Photoelectron spectroscopy experiments were conducted using a monochromatized Al Kα (1486.6 eV) source and He I (21.2 eV) excitation source for UPS and XPS, respectively, under a pressure of 5×10^{-8} Torr and an energy resolution of 0.1 eV. The secondary cut-off in the UPS spectra was used to analyze the work functions (WFs) of materials using the following equation: WF = 21.22 eV–secondary cut-off. The difference between the

valence band maximum and the Fermi level was determined through the curve fitting of the low binding energy region.

The noise current spectra of the photodetectors were measured using a pre-amplifier (SRS 570, Stanford Research Systems) connected to a lock-in amplifier (SR 530, Stanford Research Systems). The noise current was amplified by the pre-amplifier, and then recorded by the lock-in amplifier. The bias on the device was provided by the pre-amplifier. The noise current was measured versus various frequencies, as triggered by a function generator (DG 2401A, Rigol). The noise current of the device was obtained by subtracting the background noise from the total noise.

Supporting Information

Supporting Information is available from the Wiley Online Library or from the author.

Acknowledgements

B.K.J. and H.K.W contributed equally to this work. This research was supported by the Korea Electric Power Corporation (KEPCO) (R21XA01-21). This work was also supported by Samsung Electronics Co., Ltd (IO201210-08027-01)

Conflict of Interest

The authors declare no conflict of interest.

Data Availability Statement

Research data are not shared.

Keywords

colloidal quantum dots, dark currents, infrared photodiodes, minority carriers, passivation treatments, trap site densities

Received: August 5, 2021
Revised: September 27, 2021
Published online: November 9, 2021

[1] E. H. Sargent, *Nat. Photonics* **2012**, *6*, 133.
[2] J. H. Song, S. Jeong, *Nano Convergence* **2017**, *4*, 21.
[3] H. Choi, J. H. Ko, Y. H. Kim, S. Jeong, *J. Am. Chem. Soc.* **2013**, *135*, 5278.
[4] D. Kufer, I. Nikitskiy, T. Lasanta, G. Navickaite, F. H. L. Koppens, G. Konstantatos, *Adv. Mater.* **2015**, *27*, 176.
[5] D. K. Hwang, Y. T. Lee, H. S. Lee, Y. J. Lee, S. H. Shokouh, J. H. Kyhm, J. Lee, H. H. Kim, T. H. Yoo, S. H. Nam, D. I. Son, B. K. Ju, M. C. Park, J. D. Song, W. K. Choi, S. Im, *NPG Asia Mater* **2016**, *8*, e233.
[6] I. Nikitskiy, S. Goossens, D. Kufer, T. Lasanta, G. Navickaite, F. H. L. Koppens, G. Konstantatos, *Nat. Commun.* **2016**, *7*, 11954.
[7] K. Qiao, H. Deng, X. Yang, D. Dong, M. Li, L. Hu, H. Liu, H. Song, J. Tang, *Nanoscale* **2016**, *8*, 7137.
[8] A. De Iacovo, C. Venettacci, L. Colace, L. Scopa, S. Foglia, *Sci. Rep.* **2016**, *6*, 37913.
[9] Y. Wang, Z. Liu, N. Huo, F. Li, M. Gu, X. Ling, Y. Zhang, K. Lu, L. Han, H. Fang, A. G. Shulga, Y. Xue, S. Zhou, F. Yang, X. Tang, J. Zheng, M. A. Loi, G. Konstantatos, W. Ma, *Nat. Commun.* **2019**, *10*, 5136.
[10] I. Ramiro, O. Özdemir, S. Christodoulou, S. Gupta, M. Dalmases, I. Torre, G. Konstantatos, *Nano Lett.* **2020**, *20*, 1003.
[11] M. Vafaie, J. Z. Fan, A. M. Najarian, O. Ouellette, L. K. Sagar, K. Bertens, B. Sun, F. P. G. de Arquer, E. H. Sargent, *Matter* **2021**, *4*, 1042.
[12] R. Sliz, M. Lejay, J. Z. Fan, M. J. Choi, S. Kinge, S. Hoogland, T. Fabritius, F. P. G. de Arquer, E. H. Sargent, *ACS Nano* **2019**, *13*, 11988.
[13] M. Biondi, M. J. Choi, S. Lee, K. Bertens, M. Wei, A. R. Kirmani, G. Lee, H. T. Kung, L. J. Richter, S. Hoogland, Z. H. Lu, F. P. G. de Arquer, E. H. Sargent, *ACS Energy Lett.* **2021**, *6*, 468.
[14] Y. Cho, B. Hou, J. Lim, S. Lee, S. Pak, J. Hong, P. Giraud, A. R. Jang, Y. W. Lee, J. Lee, J. E. Jang, H. J. Snaith, S. M. Morris, J. I. Sohn, S. Cha, J. M. Kim, *ACS Energy Lett.* **2018**, *3*, 1036.
[15] H. K. Woo, M. S. Kang, T. Park, J. Bang, S. Jeon, W. S. Lee, J. Ahn, G. Cho, D. K. Ko, Y. Kim, D. H. Ha, S. J. Oh, *Nanoscale* **2019**, *11*, 17498.
[16] X. Zhang, E. M. J. Johansson, *J. Mater. Chem. A* **2017**, *5*, 303.
[17] B. Sun, O. Ouellette, F. P. G. de Arquer, O. Voznyy, Y. Kim, M. Wei, A. H. Proppe, M. I. Saidaminov, J. Xu, M. Liu, P. Li, J. Z. Fan, J. W. Jo, H. Tan, F. Tan, S. Hoogland, Z. H. Lu, S. O. Kelley, E. H. Sargent, *Nat. Commun.* **2018**, *9*, 4003.
[18] M. J. Choi, F. P. G. de Arquer, A. H. Proppe, A. Seifitokaldani, J. Choi, J. Kim, S. W. Baek, M. Liu, B. Sun, M. Biondi, B. Scheffel, G. Walters, D. H. Nam, J. W. Jo, O. Ouellette, O. Voznyy, S. Hoogland, S. O. Kelley, Y. S. Jung, E. H. Sargent, *Nat. Commun.* **2020**, *11*, 103.
[19] M. Liu, F. Che, B. Sun, O. Voznyy, A. Proppe, R. Munir, M. Wei, R. Quintero-Bermudez, L. Hu, S. Hoogland, A. Mandelis, A. Amassian, S. O. Kelley, F. P. G. de Arquer, E. H. Sargent, *ACS Energy Lett.* **2019**, *4*, 1225.
[20] Y. Xia, S. Liu, K. Wang, X. Yang, L. Lian, Z. Zhang, J. He, G. Liang, S. Wang, M. Tan, H. Song, D. Zhang, J. Gao, J. Tang, M. C. Beard, J. Zhang, *Adv. Funct. Mater.* **2020**, *30*, 1907379.
[21] J. P. Clifford, G. Konstantatos, K. W. Johnston, S. Hoogland, L. Levina, E. H. Sargent, *Nat. Nanotechnol.* **2009**, *4*, 40.
[22] C. Dong, S. Liu, N. Barange, J. Lee, T. Pardue, X. Yi, S. Yin, F. So, *ACS Appl. Mater. Interfaces* **2019**, *11*, 44451.
[23] S. W. Baek, O. Ouellette, J. W. Jo, J. Choi, K. W. Seo, J. Kim, B. Sun, S. H. Lee, M. J. Choi, D. H. Nam, L. N. Quan, J. Kang, S. Hoogland, F. P. G. de Arquer, J. Y. Lee, E. H. Sargent, *ACS Energy Lett.* **2018**, *3*, 2908.
[24] S. W. Baek, P. Molet, M. J. Choi, M. Biondi, O. Ouellette, J. Fan, S. Hoogland, F. P. G. de Arquer, A. Mihi, E. H. Sargent, *Adv. Mater.* **2019**, *31*, 1901745.
[25] S. Chen, Y. J. Wang, Q. Liu, G. Shi, Z. Liu, K. Lu, L. Han, X. Ling, H. Zhang, S. Cheng, W. Ma, *Adv. Energy Mater.* **2018**, *8*, 1701194.
[26] J. Z. Fan, M. Vafaie, K. Bertens, M. Sytnyk, J. M. Pina, L. K. Sagar, O. Ouellette, A. H. Proppe, A. S. Rasouli, Y. Gao, S. W. Baek, B. Chen, F. Laquai, S. Hoogland, F. P. G. de Arquer, W. Heiss, E. H. Sargent, *Nano Lett.* **2020**, *20*, 5284.
[27] N. Sukharevska, D. Bederak, V. M. Goossens, J. Momand, H. Duim, D. N. Dirin, M. V. Kovalenko, B. J. Kooi, M. A. Loi, *ACS Appl. Mater. Interfaces* **2021**, *13*, 5195.
[28] R. Azmi, G. Seo, T. K. Ahn, S. Y. Jang, *ACS Appl. Mater. Interfaces* **2018**, *10*, 35244.
[29] F. Yang, Y. Xu, M. Gu, S. Zhou, Y. Wang, K. Lu, Z. Liu, X. Ling, Z. Zhu, J. Chen, Z. Wu, Y. Zhang, Y. Xue, F. Li, J. Yuan, W. Ma, *J. Mater. Chem. A* **2018**, *6*, 17688.
[30] K. Bertens, J. Z. Fan, M. Biondi, A. S. Rasouli, S. Lee, P. Li, B. Sun, S. Hoogland, F. P. G. de Arquer, Z. H. Lu, E. H. Sargent, *ACS Mater. Lett.* **2020**, *2*, 1583.
[31] J. Yang, J. Lee, J. Lee, W. Yi, *J. Power Sources* **2019**, *421*, 124.

[32] K. Lu, Y. Wang, J. Yuan, Z. Cui, G. Shi, S. Shi, L. Han, S. Chen, Y. Zhang, X. Ling, Z. Liu, L. Chi, J. Fan, W. Ma, *J. Mater. Chem. A* **2017**, *5*, 23960.
[33] P. R. Brown, R. R. Lunt, N. Zhao, T. P. Osedach, D. D. Wanger, L. Y. Chang, M. G. Bawendi, V. Bulović, *Nano Lett.* **2011**, *11*, 2955.
[34] M. Ahmadi, T. Wu, B. Hu, *Adv. Mater.* **2017**, *29*, 1605242.
[35] B. V. Olson, J. K. Kim, E. A. Kadlec, J. F. Klem, S. D. Hawkins, D. Leonhardt, W. T. Coon, T. R. Fortune, M. A. Cavaliere, A. Tauke-Pedretti, E. A. Shaner, *Appl. Phys. Lett.* **2015**, *107*, 183504.
[36] N. G. Tarr, D. L. Pulfrey, *Solid-State Electron.* **1979**, *22*, 265.
[37] P. H. Rekemeyer, C. H. M. Chuang, M. G. Bawendi, S. Gradečak, *Nano Lett.* **2017**, *17*, 6221.
[38] S. C. Lee, G. L. Pearson, *J. Appl. Phys.* **1981**, *52*, 275.
[39] G. Simone, M. J. Dyson, C. H. L. Weijtens, S. C. J. Meskers, R. Coehoorn, R. A. J. Janssen, G. H. Gelinck, *Adv. Opt. Mater.* **2020**, *8*, 1901568.
[40] S. Yoon, J. Cho, K. M. Sim, J. Ha, D. S. Chung, *Appl. Phys. Lett.* **2017**, *110*, 083301.
[41] S. Valouch, C. Hönes, S. W. Kettlitz, N. Christ, H. Do, M. F. G. Klein, H. Kalt, A. Colsmann, U. Lemmer, *Org. Electron.* **2012**, *13*, 2727.
[42] H. Beygi, S. A. Sajjadi, A. Babakhani, J. F. Young, F. C. J. M. van Veggel, *Sol. Energy Mater. Sol. Cells* **2019**, *203*, 110163.
[43] Y. Kim, F. Che, J. W. Jo, J. Choi, F. P. G. de Arquer, O. Voznyy, B. Sun, J. Kim, M. J. Choi, R. Quintero-Bermudez, F. Fan, C. S. Tan, E. Bladt, G. Walters, A. H. Proppe, C. Zou, H. Yuan, S. Bals, J. Hofkens, M. B. J. Roeffaers, S. Hoogland, E. H. Sargent, *Adv. Mater.* **2019**, *31*, 1805580.
[44] X. Zhang, Y. Chen, L. Lian, Z. Zhang, Y. Liu, L. Song, C. Geng, J. Zhang, S. Xu, *Nano Res.* **2021**, *14*, 628.
[45] H. Beygi, S. A. Sajjadi, A. Babakhani, J. F. Young, F. C. J. M. van Veggel, *Appl. Surf. Sci.* **2018**, *457*, 1.
[46] M. J. Choi, S. W. Baek, S. Lee, M. Biondi, C. Zheng, P. Todorovic, P. Li, S. Hoogland, Z. H. Lu, F. P. G. de Arquer, E. H. Sargent, *Adv. Sci.* **2020**, *7*, 2000894.
[47] A. Stavrinadis, A. K. Rath, F. P. G. de Arquer, S. L. Diedenhofen, C. Magén, L. Martinez, D. So, G. Konstantatos, *Nat. Commun.* **2013**, *4*, 2981.
[48] H. Tavakoli Dastjerdi, R. Tavakoli, P. Yadav, D. Prochowicz, M. Saliba, M. M. Tavakoli, *ACS Appl. Mater. Interfaces* **2019**, *11*, 26047.
[49] W. J. E. Beek, M. M. Wienk, M. Kemerink, X. Yang, R. A. J. Janssen, *J. Phys. Chem. B* **2005**, *109*, 9505.
[50] M. Liu, O. Voznyy, R. Sabatini, F. P. G. de Arquer, R. Munir, A. H. Balawi, X. Lan, F. Fan, G. Walters, A. R. Kirmani, S. Hoogland, F. Laquai, A. Amassian, E. H. Sargent, *Nat. Mater.* **2017**, *16*, 258.